

Supplementary Information

Alumina nanoparticles enable optimal spray-coated perovskite thin film growth on self-assembled monolayers for efficient and reproducible photovoltaics

Elena J. Cassella,^{1,†} Robert D.J. Oliver,^{2,†} Timothy Thornber,¹ Sophie Tucker,^{1,3} Rehmat Goodwin,^{1,3} David G. Lidzey,^{1,*} Alexandra J. Ramadan^{1,*}

1. Department of Physics and Astronomy, University of Sheffield, Hicks Building, Hounsfield Road, Sheffield S3 7RH, United Kingdom
2. Department of Materials Science and Engineering, University of Sheffield, Sir Robert Hadfield Building, Mappin Street, Sheffield, S1 3JD, United Kingdom
3. Grantham Centre for Sustainable Futures, University of Sheffield, Sheffield S10 2TN, United Kingdom

†: these authors contributed equally

Corresponding authors: a.ramadan@sheffield.ac.uk, d.g.lidzey@sheffield.ac.uk

Table S1: Tabulated device performance for perovskite solar cells (or modules) incorporating a one-step spray-coated “triple cation” (CsFAMA) perovskite absorber layer.

Year	Active area (mm ²)	PCE (%)	Stabilized PCE (%)	Stack	Ref.
2018	2.6	17.8	17	ITO/SnO ₂ /perovskite/Spiro-OMeTAD/Au	1
2019	13	18.5	17.3	ITO/SnO ₂ /perovskite/Spiro-OMeTAD/Au	2
	100	15.07	14.3	ITO/SnO ₂ /perovskite/Spiro-OMeTAD/Au	2
2020	2.5	19.4	18.7	ITO/SnO ₂ /perovskite/Spiro-OMeTAD/Au	3
	15.4	16.3	16.3	ITO/SnO ₂ /perovskite/Spiro-OMeTAD/Au	3
	108	12.7	12.5	ITO/SnO ₂ /perovskite/Spiro-OMeTAD/Au	3
2020	13	20.6	Not reported	ITO/SnO ₂ /perovskite/Spiro-OMeTAD/Au	4
2022	1080*	10.66	9	ITO/SnO ₂ /perovskite/Spiro-OMeTAD/Au	5
2023	7.8 [#]	18.24	16.56	PEN/ITO/PTAA/perovskite/C60/BCP/Cu	6
	3510* [#]	16.1	Not reported	PEN/ITO/PTAA/perovskite/C60/BCP/Cu	6
This Work	2	20.1	20.3	ITO/Me-4PACz/Al₂O₃-nps/perovskite/C₆₀/BCP/Ag	
	20	20.4	20.2	ITO/Me-4PACz/Al₂O₃-nps/perovskite/C₆₀/BCP/Ag	
	100	17.1	17.2	ITO/Me-4PACz/Al₂O₃-nps/perovskite/C₆₀/BCP/Ag	

* Perovskite minimodule

[#] Flexible substrate

Table S2: Tabulated device performance for inverted (*p-i-n*) configuration perovskite solar cells (or modules) incorporating a one-step spray-coated perovskite absorber layer.

Year	Active area (mm ²)	PCE (%)	Stabilized PCE (%)	Stack	Ref.
2014	2.5	11.1	not reported	ITO/PEDOT:PSS/MAPbI _{3-x} Cl _x /PCBM/Ca/Al	7
2015	10	10.2	not reported	ITO/PEDOT:PSS/MAPbI ₃ /C ₆₀ /BCP/Al	8
	60	6.88	not reported	ITO/PEDOT:PSS/MAPbI ₃ /C ₆₀ /BCP/Al	8
	342	4.66	not reported	ITO/PEDOT:PSS/MAPbI ₃ /C ₆₀ /BCP/Al	8
2016	2.5	11.4	not reported	ITO/PEDOT:PSS/MAPbI _{3-x} Cl _x /PCBM/LiF/Al	9
2017	1.77	13.3	13	ITO/PEDOT:PSS/MAPbI ₃ /C ₆₀ /BCP/LiF/Al	10
2017	10	15.4	not reported	ITO/PEDOT:PSS/MAPbI ₃ /PCBM/C ₆₀ /Al	11
2018	4	12.6	11.6	ITO/PEDOT:PSS/MAPbI ₃ /PCBM/Ag	12
2018	4	14.2	13.1	ITO/PEDOT:PSS/MAPbI _{3-x} Cl _x /PCBM/PEIE/Ag	13
2018	100	12.3	not reported	ITO/PEDOT:PSS/MAPbI ₃ /C ₆₀ /BCP/Ag	14
	200	10.18	not reported	ITO/PEDOT:PSS/MAPbI ₃ /C ₆₀ /BCP/Ag	14
	300	7.01	not reported	ITO/PEDOT:PSS/MAPbI ₃ /C ₆₀ /BCP/Ag	14
2019	7.54	16.9	not reported	ITO/PEDOT:PSS/MAPbI ₃ /C ₆₀ /BCP/Cu	15
	100	14.2	13.1	ITO/PEDOT:PSS/MAPbI ₃ /C ₆₀ /BCP/Cu	15
2019	9	15.61	not reported	FTO/NiOx/FA0.25MA0.75PbI ₃ /C ₆₀ /BCP/Ag	16
2020	100	13.76	not reported	TO/NiOx/MAPbI ₃ /C ₆₀ /PCBM:PNDI(2OD)T2/Ag	17
2020	20	18	not reported	ITO/NiOx/(Cs _{0.17} FA _{0.83})PbI ₃ /C ₆₀ /BCP/Ag	18
	200	15.5*	not reported	ITO/NiOx/(Cs _{0.17} FA _{0.83})PbI ₃ /C ₆₀ /BCP/Ag	18
	590	15.2*	15	ITO/NiOx/(Cs _{0.17} FA _{0.83})PbI ₃ /C ₆₀ /BCP/Ag	18
2021	9	17.07	not reported	ITO/NiOx/MAPbI _{3-x} Brx/C ₆₀ /BCP/Ag	19
2021	1040	6.48*	5.32	ITO/NiOx/MAPbI ₃ /C ₆₀ /BCP/Ag	20
2022	9	17.18	not reported	ITO/NiOx/MAPbI _{3-x} Brx/C ₆₀ /BCP/Ag	21

2022	2.5	18.3	not reported	ITO/MeO-2PACz/MAPbI3/C60/BCP/Ag	22
	2.5	20.8 [†]	20.5	ITO/MeO-2PACz/MAPbI3/C60/BCP/Ag	22
2023	7.8	18.24 [‡]	16.56	PEN/ITO/PTAA/perovskite/C60/BCP/Cu	6
	3510	16.1 ^{‡*}	Not reported	PEN/ITO/PTAA/perovskite/C60/BCP/Cu	6
2023	12.5	14.8	Not reported	ITO/NiOx/Cs0.18FA0.82Pb(I0.94Br0.06)3 /LiF/C60/BCP/Cu	23
2024	8.9	20.32	not reported	/ITO/NiOx/MeO-2PACz/MAPbI3/PCBM/BCP/Ag	24
This Work	2	20.1	20.3	ITO/Me-4PACz/Al₂O₃-nps/perovskite/C₆₀/BCP/Ag	
	20	20.4	20.2	ITO/Me-4PACz/Al₂O₃-nps/perovskite/C₆₀/BCP/Ag	
	100	17.1	17.2	ITO/Me-4PACz/Al₂O₃-nps/perovskite/C₆₀/BCP/Ag	

* Perovskite minimodule

[‡] Flexible substrate

[†] Devices have an anti-reflective coating

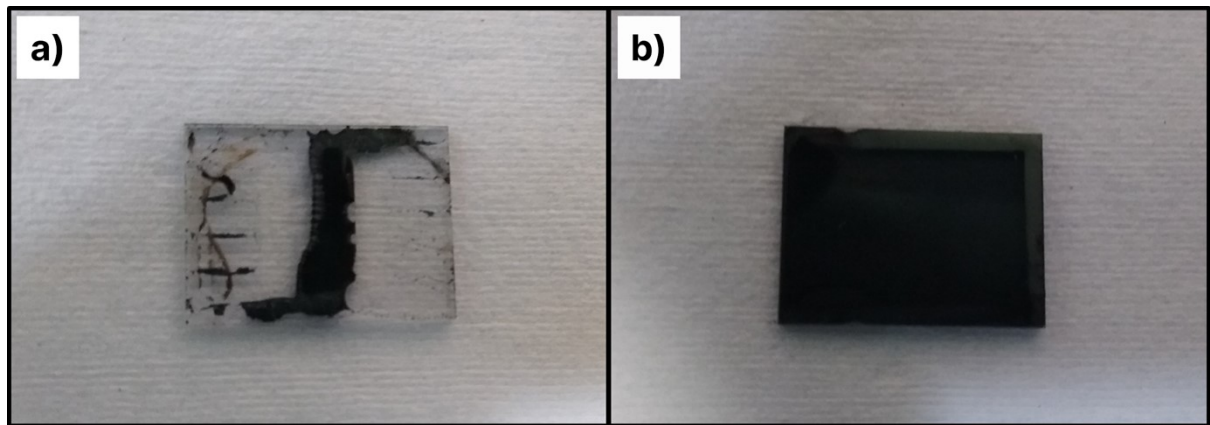


Figure S1: Representative photographs of spin-coated $\text{Cs}_{0.05}\text{FA}_{0.81}\text{MA}_{0.14}\text{PbI}_{2.55}\text{Br}_{0.45}$ thin films on (a) neat Me-4PACz thin films and (b) with a dilute (1:200) Al_2O_3 nanoparticle (nanoparticle to isopropanol) modification interlayer both on indium tin oxide coated glass.

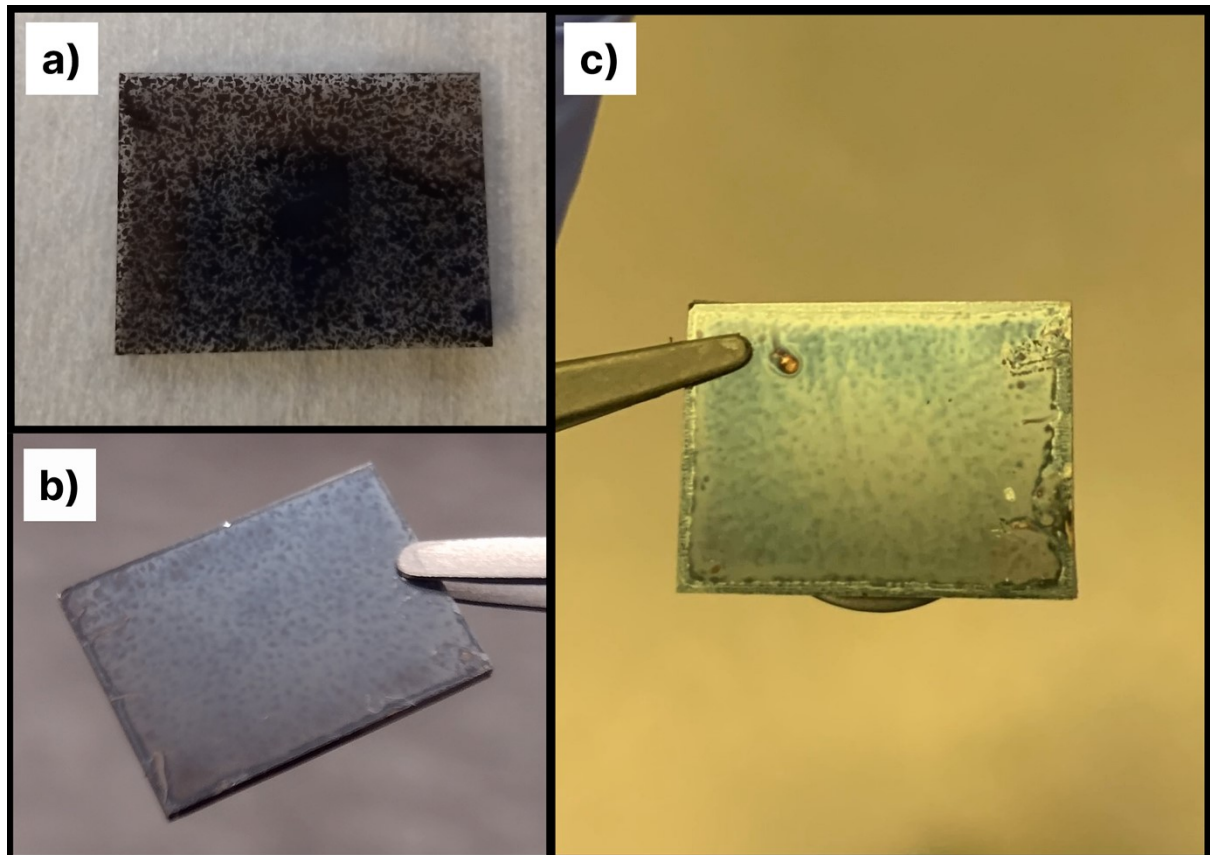


Figure S2: Representative photographs of spray-coated $\text{Cs}_{0.05}\text{FA}_{0.81}\text{MA}_{0.14}\text{PbI}_{2.55}\text{Br}_{0.45}$ thin films on Me-4PACz thin films modified with (a) 1:200 dilution, (b) 1:100 dilution and (c) 1:50 dilution of Al_2O_3 nanoparticle solution to isopropanol all on indium tin oxide coated glass.

	Bare Me-4PACz			1:200			1:100			1:50		
Contact Angle (°)	Left	Right	Avg.	Left	Right	Avg.	Left	Right	Avg.	Left	Right	Avg.
75.8	72.3	74.1	69.7	69.4	69.6	65.7	65	65.3	51.8	47.6	49.7	
80.5	70.2	75.3	72.7	71.3	72.0	69.3	70.2	69.8	50.5	52.5	51.5	
81.4	74.4	77.9	69.4	69.5	69.5	72.2	72.5	72.3	51.8	48.2	50.0	
72.6	71.8	72.2	69.7	67.5	68.6	64.6	61.9	63.2	49.0	46.0	47.5	
77.8	73.9	75.8	61.1	63.6	62.3	59.8	65.3	62.6	36.8	44.7	40.7	
72.4	69.6	71.0	72.8	75.6	74.2	65.4	65.3	65.3	53.3	49.7	51.5	
81.8	69.7	75.8				66.2	65.0	65.6	43.5	43.3	43.4	
72.5	69.8	71.1				65.8	64.8	65.3	42.0	45.2	43.6	
71.3	69.1	70.2				64.3	63.8	64.0				
Mean Angle (°)	73.7			69.4			65.9			47.2		
Standard Deviation	2.70			3.99			3.14			4.16		

Table S3: Full data set for contact angle measurements of water onto Al₂O₃ nanoparticle modified Me-4PACz thin films on indium tin oxide glass.

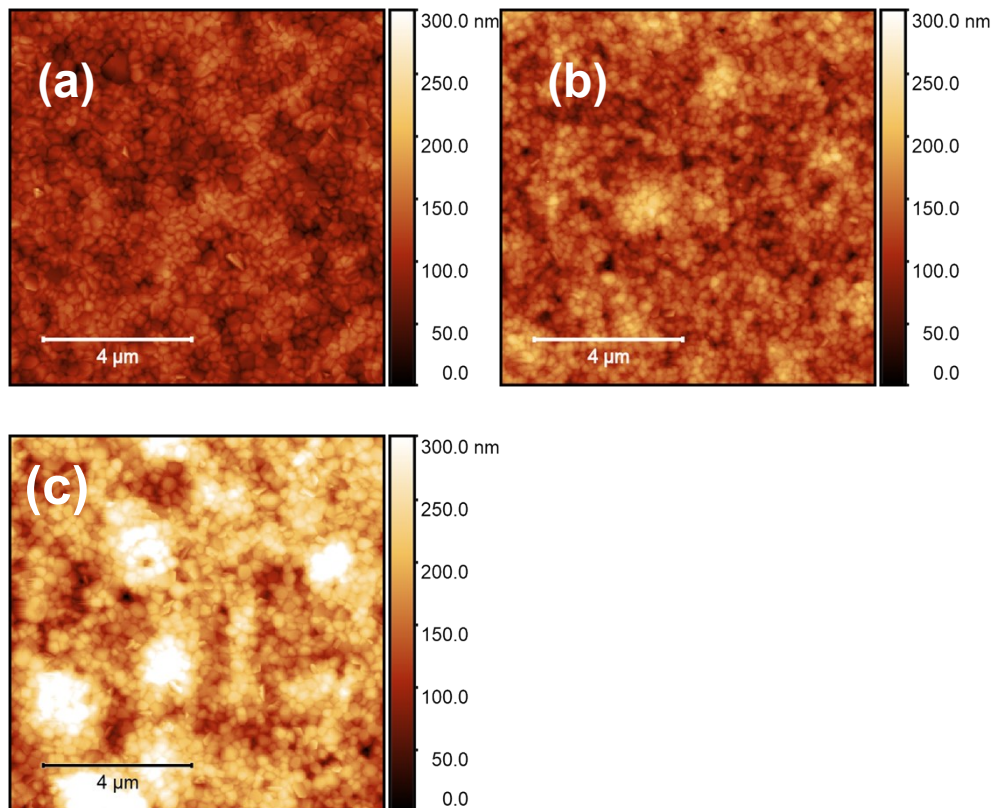


Figure S3: Atomic force microscopy (AFM) images of $\text{Cs}_{0.05}\text{FA}_{0.81}\text{MA}_{0.14}\text{PbI}_{2.55}\text{Br}_{0.45}$ thin films on Al_2O_3 treated Me-4PACz on indium tin oxide (ITO) glass. The perovskite thin films were fabricated through spin- or spray-coating and the ratios represent dilution of nanoparticles: isopropanol. (a) 1:100 spin-coating (b) 1:100 spray-coating and (c) 1:50 spray-coating.

	Spray 1:100	Spray 1:50	Spin 1:100
Roughness (nm)	32.3	51.0	24.5
	30.1	26.6	23.9
	30.6	53.9	22.3
	29.7	54.3	23.5
	38.1	38.9	23.2
Mean Roughness (nm)	32.2	44.9	23.5
Standard Deviation	3.46	12.0	0.83

Table S4: Roughness data extracted from atomic force microscopy images using Gwyddion software.

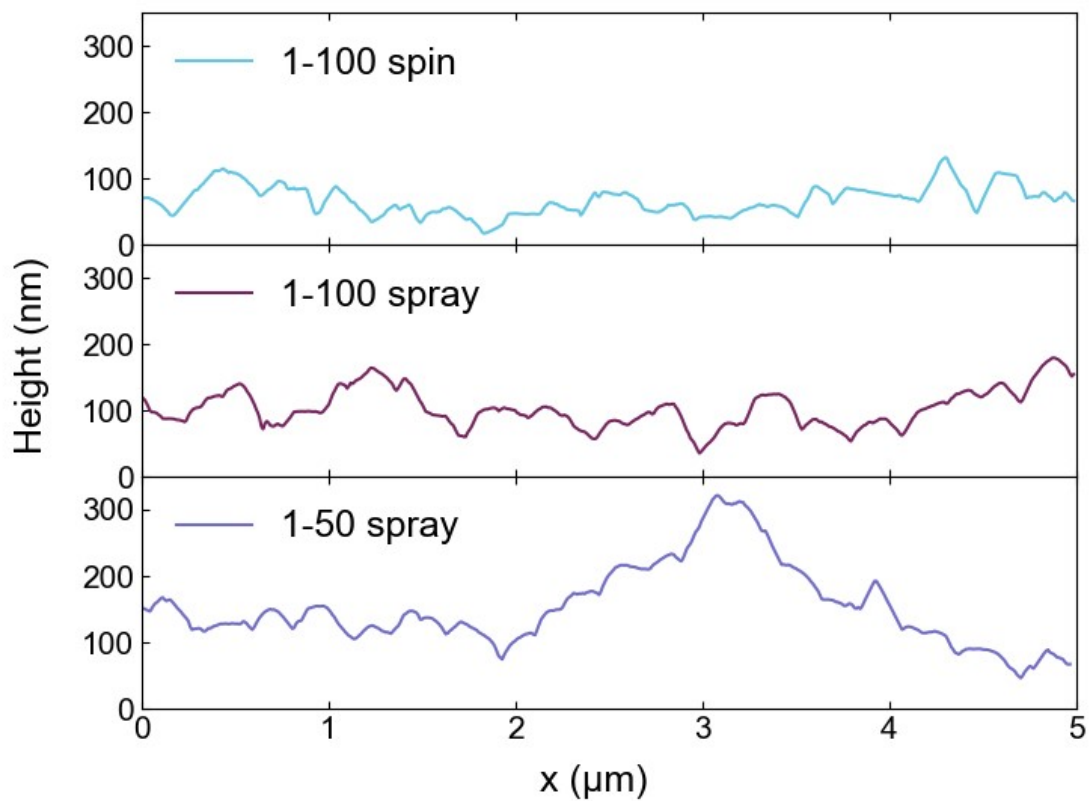


Figure S4: Line profiles from $5 \mu\text{m}$ atomic force microscopy images (shown in Figure 2) of $\text{Cs}_{0.05}\text{FA}_{0.81}\text{MA}_{0.14}\text{PbI}_{2.55}\text{Br}_{0.45}$ thin films on Al_2O_3 treated Me-4PACz on indium tin oxide (ITO) glass.

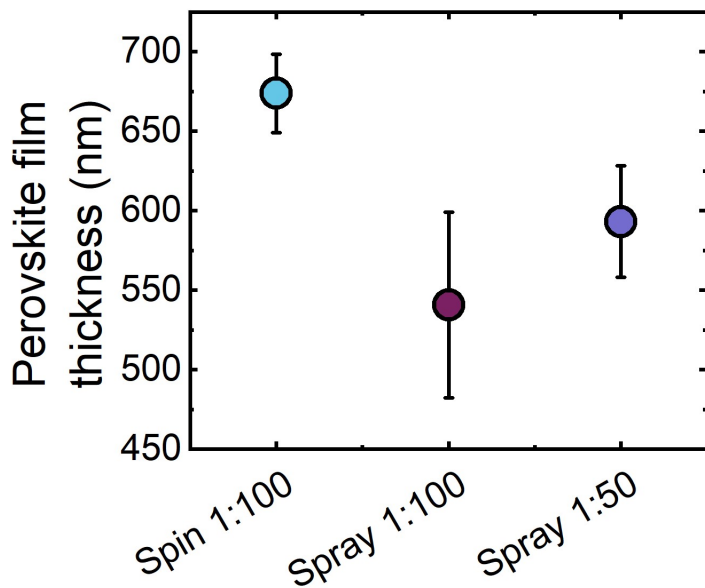


Figure S5: Profilometer measured thickness of $\text{Cs}_{0.05}\text{FA}_{0.81}\text{MA}_{0.14}\text{PbI}_{2.55}\text{Br}_{0.45}$ thin films on Al_2O_3 treated Me-4PACz on indium tin oxide (ITO) glass. Fabrication method and dilution of alumina nanoparticles (alumina:isopropanol) is indicated on the x-axis. Error bars represent the mean standard deviation (+/-) ($n = 5$ for each).

	Spin 1:100	Spray 1:100	Spray 1:50
Film Thickness (nm)	681	596	613
	683	589	638
	695	497	559
	631	463	599
	679	558	557
Mean Thickness (nm)	674	541	593
Standard Deviation	25	58	35

Table S5: Profilometer measured thin film thickness of $\text{Cs}_{0.05}\text{FA}_{0.81}\text{MA}_{0.14}\text{PbI}_{2.55}\text{Br}_{0.45}$ thin films on Al_2O_3 treated Me-4PACz on indium tin oxide (ITO) glass.

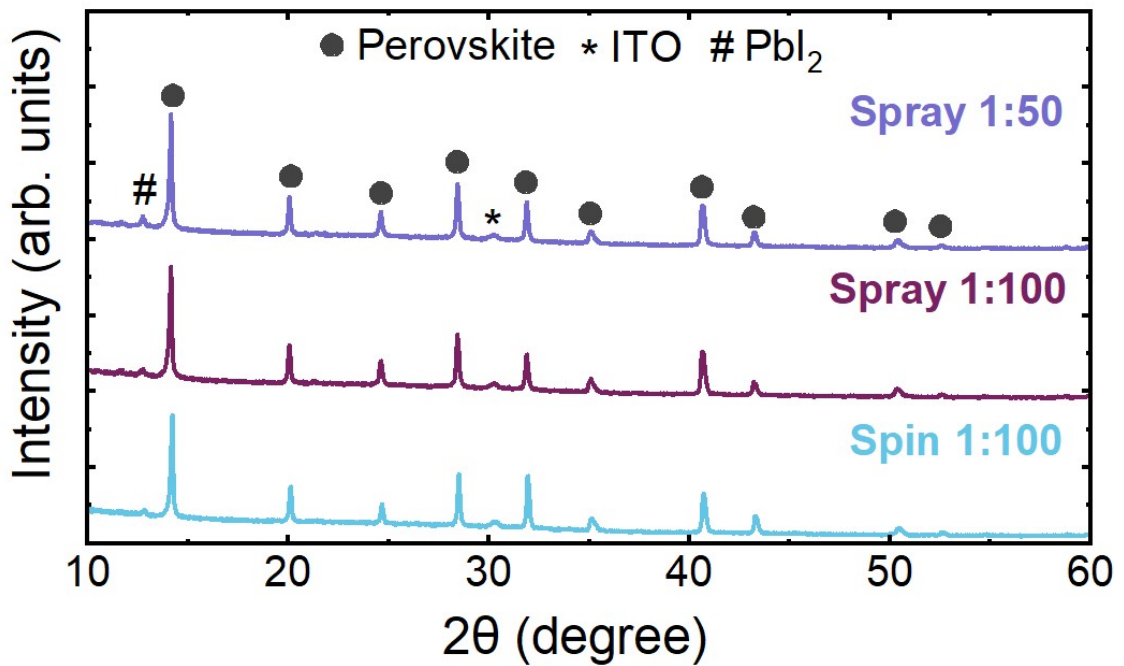


Figure S6: X-ray diffraction patterns with extended range for $\text{Cs}_{0.05}\text{FA}_{0.81}\text{MA}_{0.14}\text{PbI}_{2.55}\text{Br}_{0.45}$ thin films on Al_2O_3 treated Me-4PACz on indium tin oxide (ITO) glass.

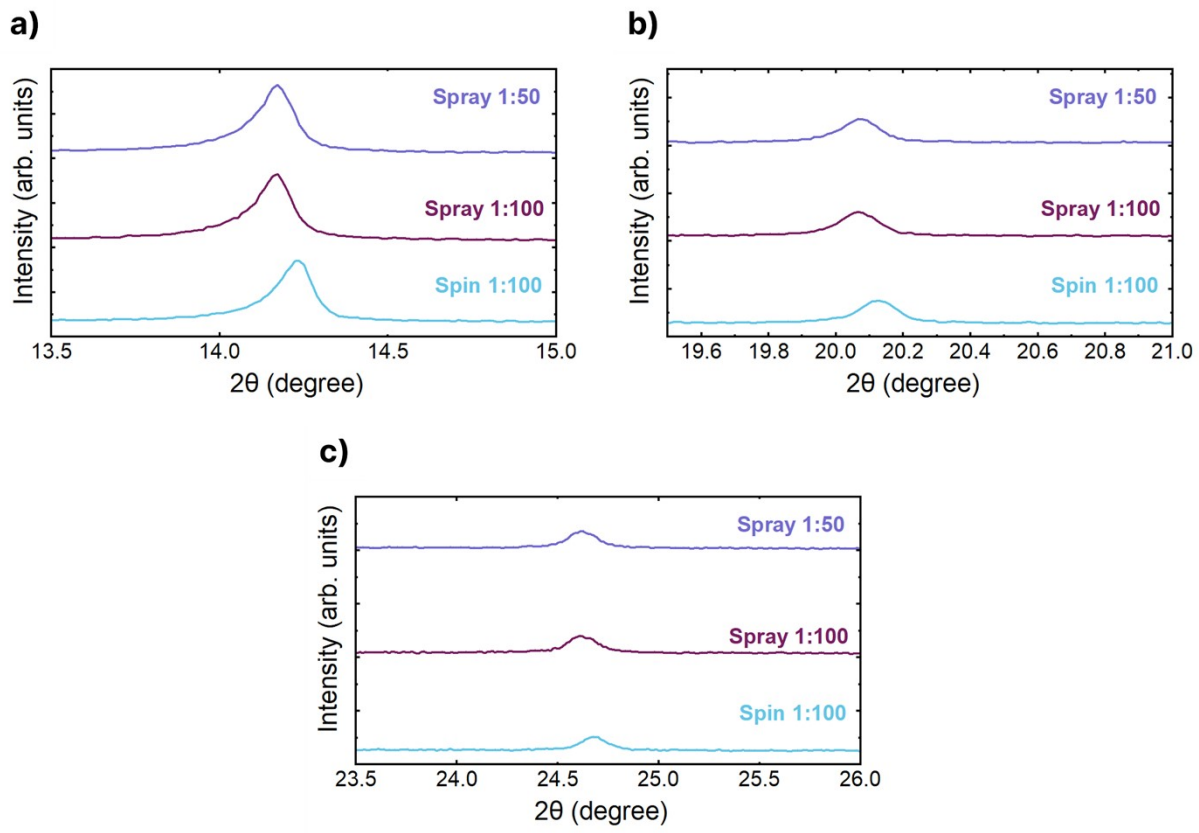


Figure S7: X-ray diffraction patterns expansions around $2\theta \sim 14^\circ$, $\sim 20^\circ$ and $\sim 25^\circ$ for $\text{Cs}_{0.05}\text{FA}_{0.81}\text{MA}_{0.14}\text{PbI}_{2.55}\text{Br}_{0.45}$ thin films on Al_2O_3 treated Me-4PACz on indium tin oxide (ITO) glass.

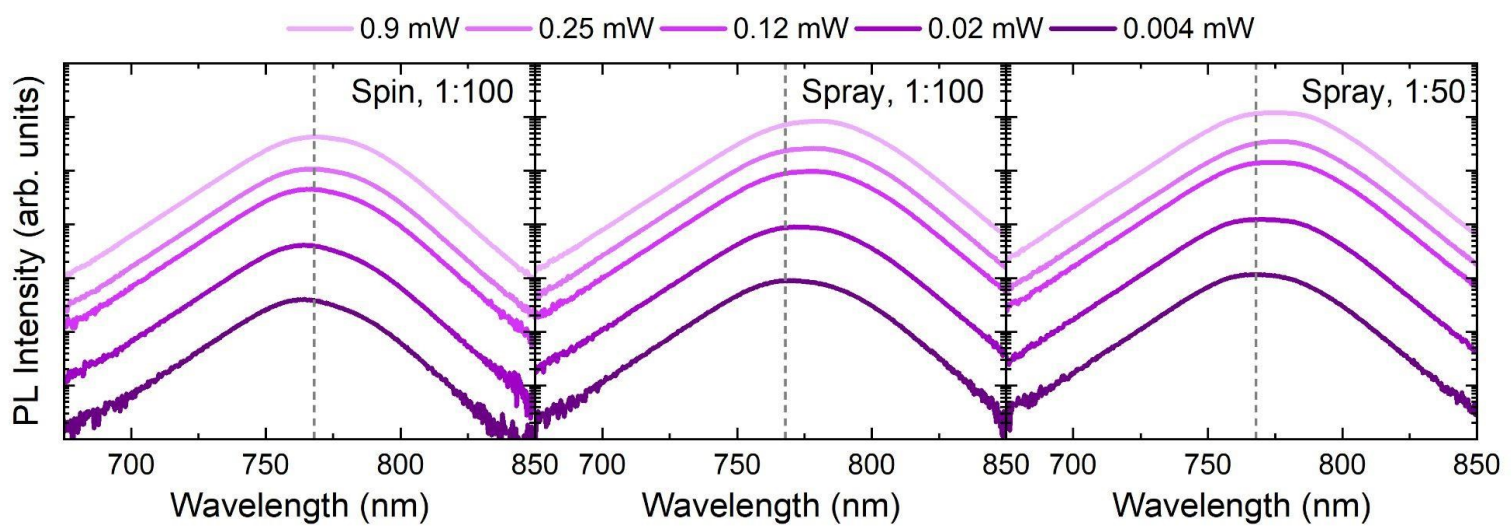


Figure S8: Intensity dependent steady-state photoluminescence spectra presented on a logarithmic intensity scale of $\text{Cs}_{0.05}\text{FA}_{0.81}\text{MA}_{0.14}\text{PbI}_{2.55}\text{Br}_{0.45}$ thin films on Al_2O_3 treated Me-4PACz on indium tin oxide (ITO) glass.

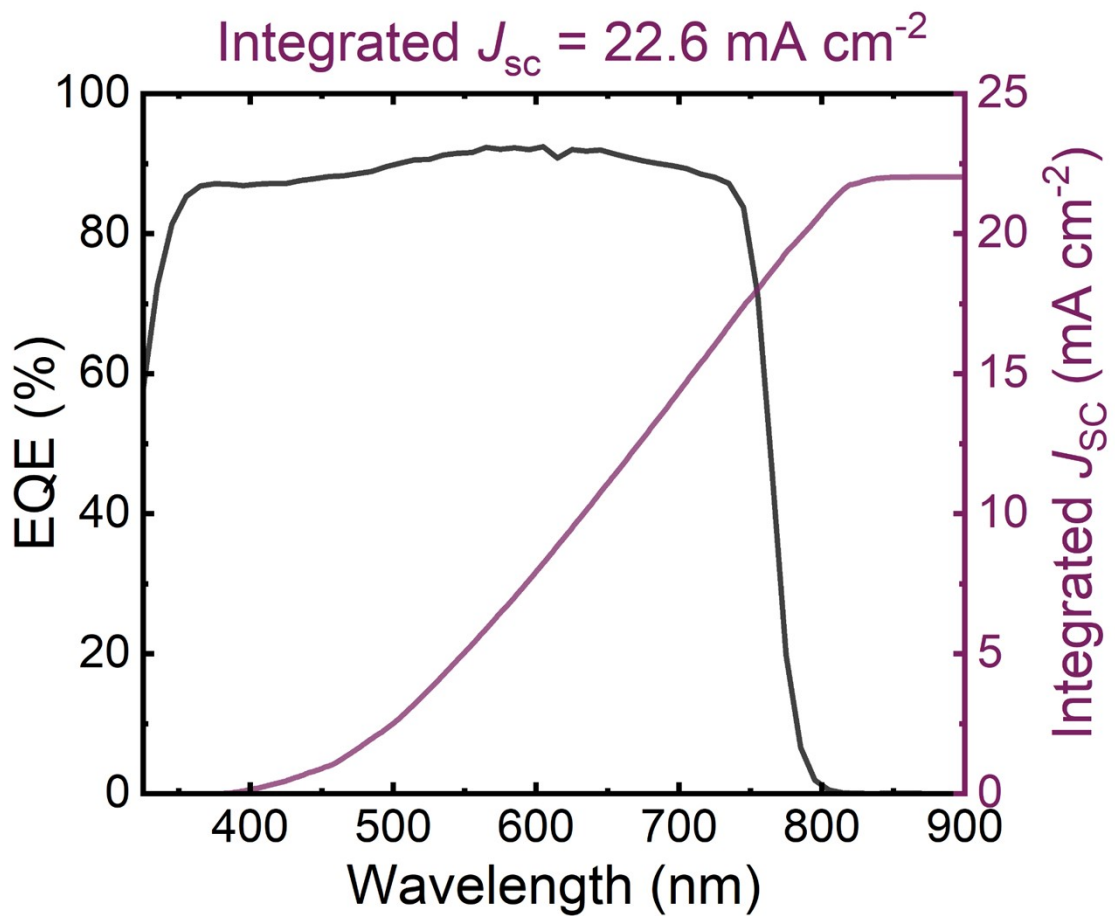


Figure S9: External quantum efficiency (EQE) and integrated short circuit current density for the champion spray-coated (1:100) 0.02 cm^2 photovoltaic device. The integrated short circuit current is in good agreement with the measured J_{SC} . The J_{SC} determined from JV curves is 23.3 mA cm^{-2} and the integrated J_{SC} is 22.6 mA cm^{-2} .

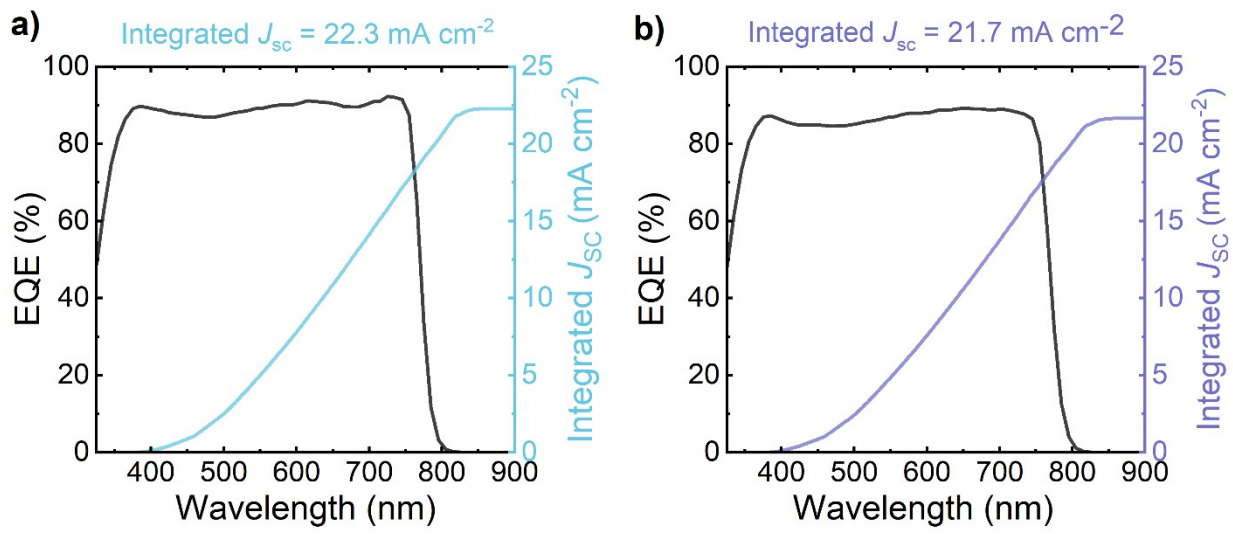


Figure S10: External quantum efficiency (EQE) and integrated short circuit current density for (a) spin 1:100 and (b) spray 1:50 spray-coated 0.02 cm^2 photovoltaic devices. The integrated short circuit currents are in good agreement with the measured J_{SC} .

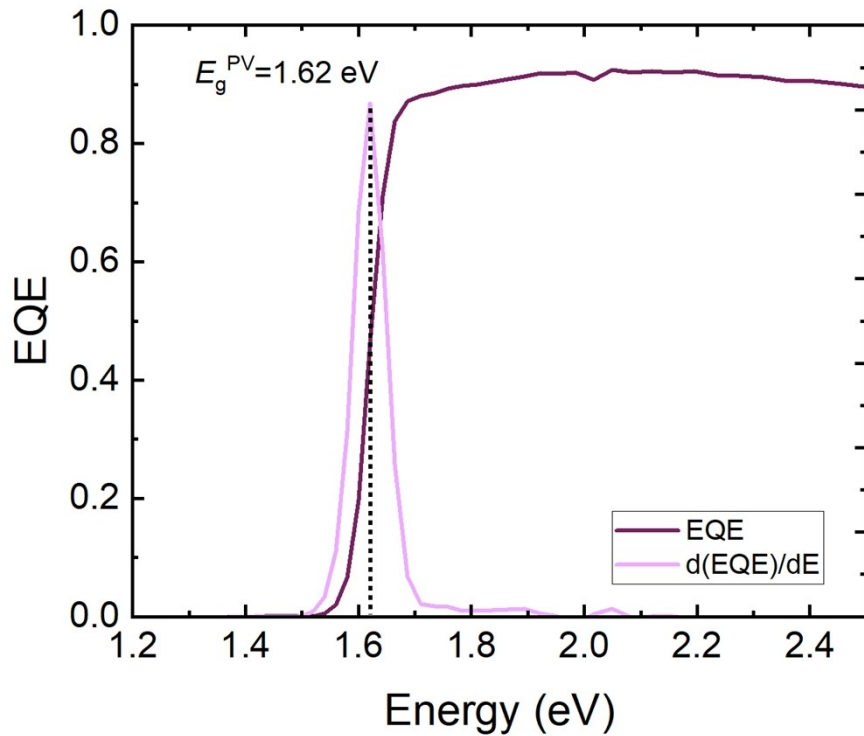


Figure S11: Calculated photovoltaic bandgap (E_g^{PV}) for the champion spray-coated (1:100) 0.02 cm² photovoltaic device from external quantum efficiency measurements.

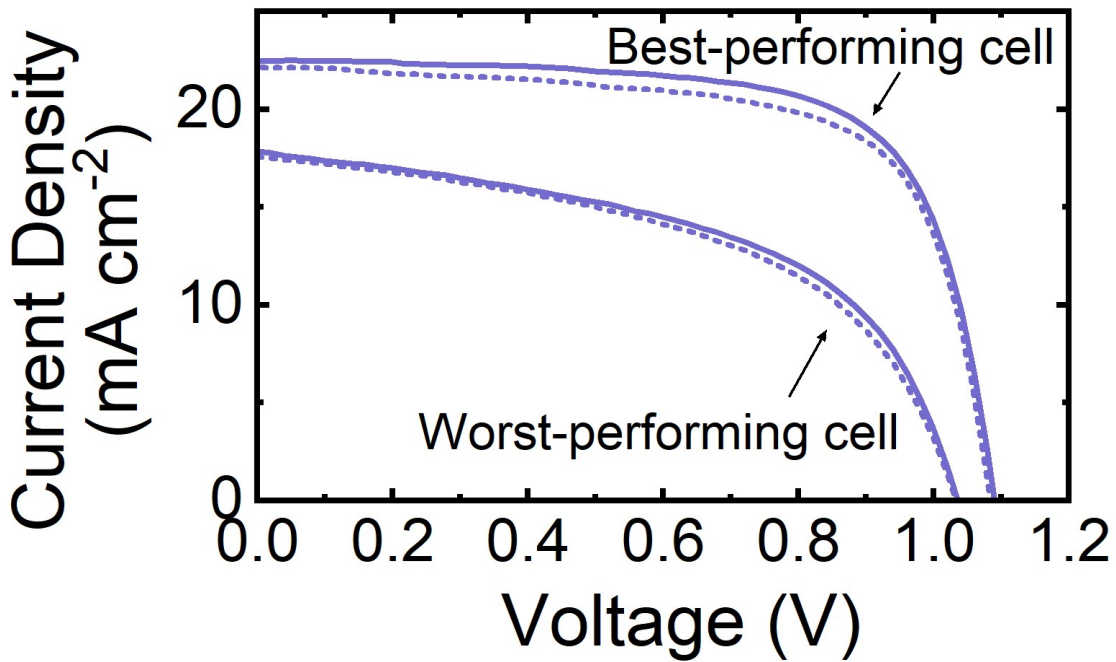


Figure S12: Comparison of the measured *JV* curves for both the best and worst performing devices incorporating the spray 1:50 Al₂O₃ nanoparticle condition. This comparison highlights the considerable resistive losses possible for this interlayer condition.

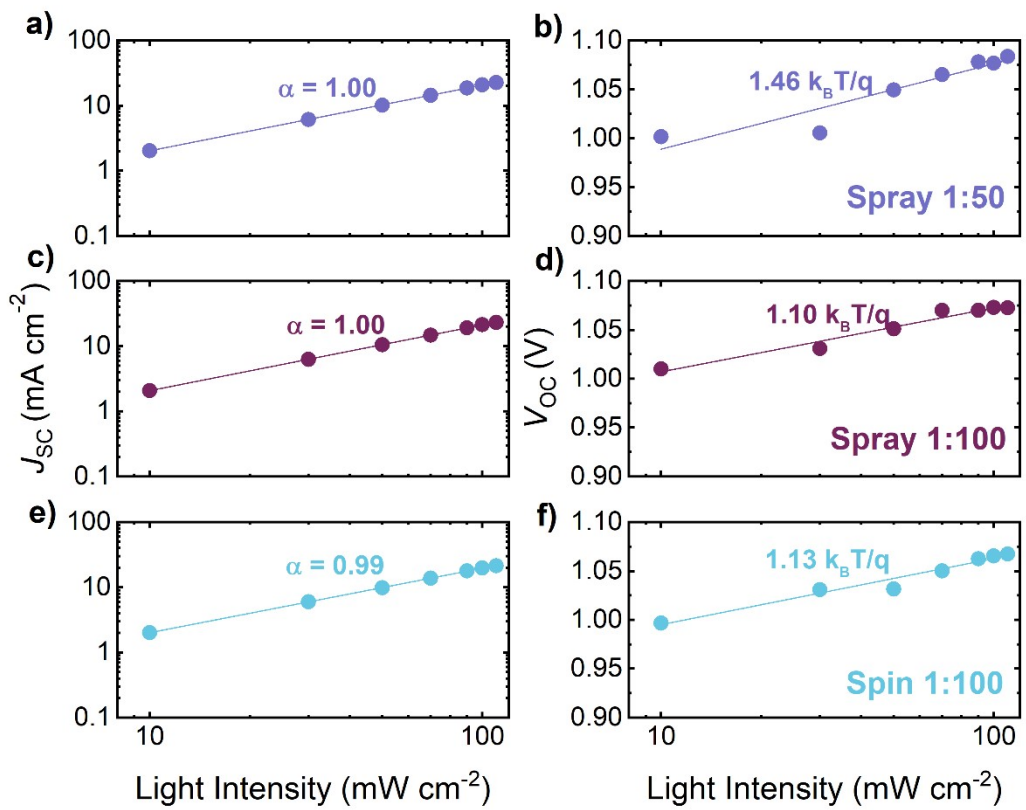


Figure S13: Light intensity dependent JV characteristics of spray 1:50 (a, b), spray 1:100 (c,d), and spray 1:50 (e,f) photovoltaic devices. (b,d,f) show the light-dependent V_{OC} response of spray 1:50, spray 1:100, and spin 1:100 cells, having n values of 1.46, 1.10, and 1.13 $k_B T/q$ respectively.

Supplementary Note 1

According to the power law $J_{SC} \propto I^\alpha$, where I is the incident light intensity, **Supplementary Figure 13 (a,c,e)** show a double logarithmic plot of J_{SC} versus light intensity for spray 1:50, Spray 1:100, and Spin 1:100 cells, respectively. All cells demonstrate an α value of ~ 1.00 indicating that there is no space charge effect limiting the device photocurrent.²⁵ The Al₂O₃-np interlayer has not introduced a charge extraction barrier at the hole-transporting interface.

To evaluate the recombination behavior in full devices, the dependence of device V_{OC} against light intensity was investigated. Diode ideality factors (n) for each device type were determined from a linear fit of the semilogarithmic plot of V_{OC} against light intensity according to²⁶

$$n = \frac{q}{k_B T d(\ln(I))} \quad \text{#Equation 1}$$

where q is the elementary charge, $k_B T$ is thermal energy, and I is the light intensity. The slope of the linear fit is indicative of the recombination mechanisms occurring within the devices. Further details can be found in Ref ³¹

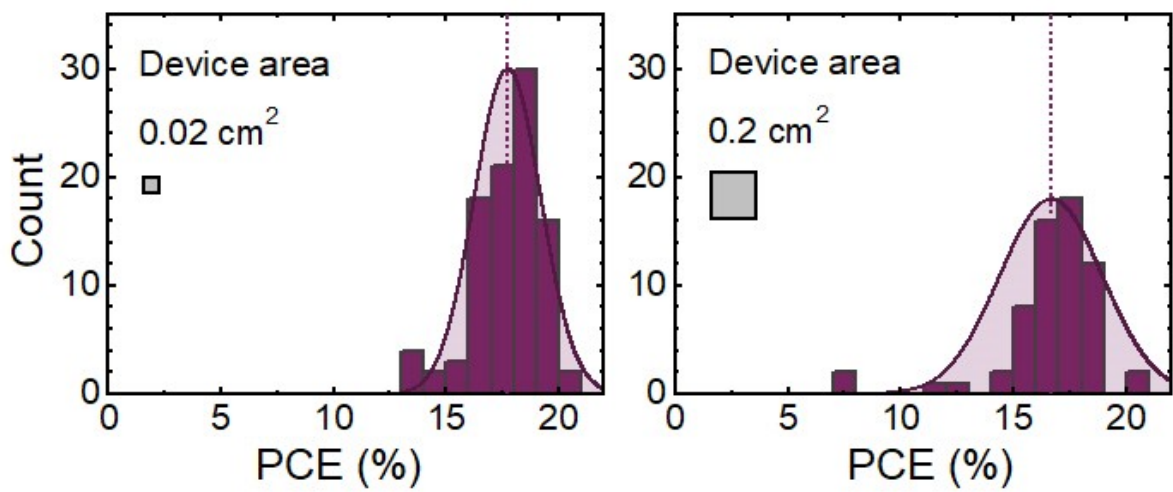


Figure S14: Histogram plots showing the distribution of power conversion efficiency values for the different active device areas. Despite an order of magnitude increase in active device area the measured power conversion efficiencies remain consistent.

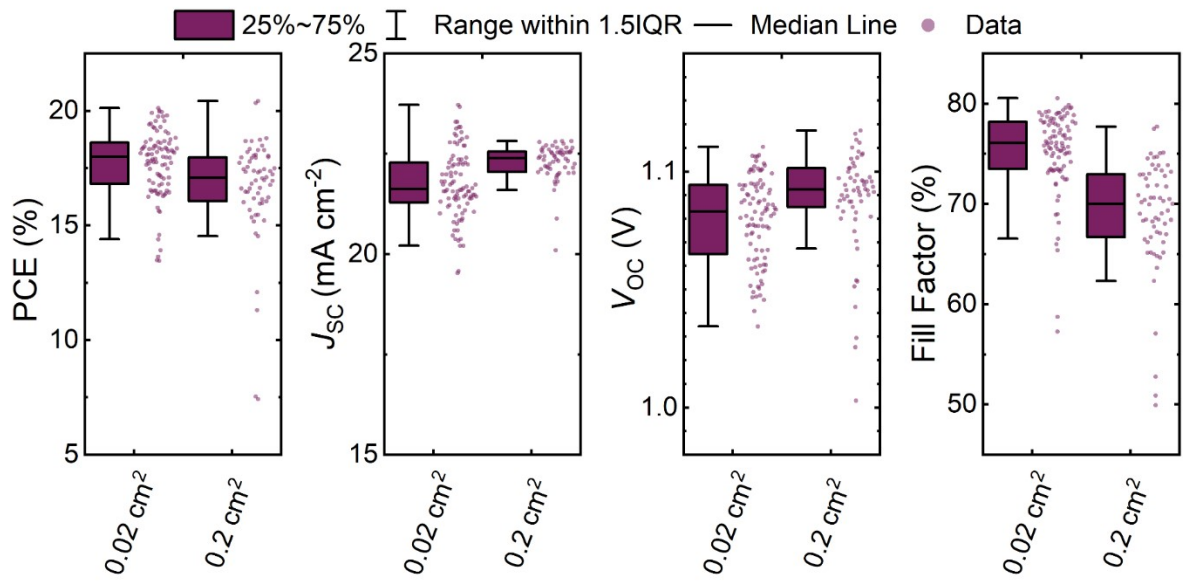


Figure S15: Box plots representing measured device performance characteristics for $\text{Cs}_{0.05}\text{FA}_{0.81}\text{MA}_{0.14}\text{PbI}_{2.55}\text{Br}_{0.45}$ photovoltaic devices incorporating the (1:100) Al_2O_3 nanoparticle interlayer to facilitate wetting on top of Me-4PACz.

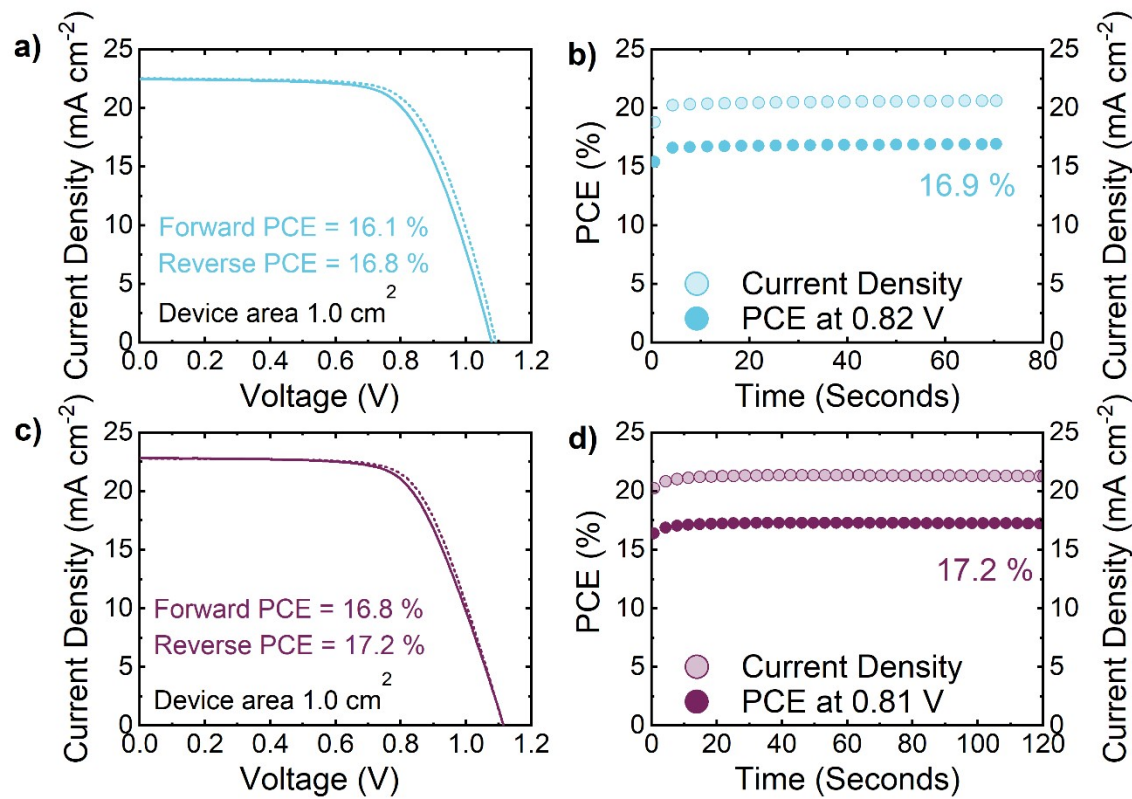


Figure S16: *JV* characteristics for 1 cm² device active area and corresponding stabilised power conversion efficiency at maximum power point for (a-b) spin 1:100 and (c-d) spray 1:100.

References

- 1 J. E. Bishop, J. A. Smith, C. Greenland, V. Kumar, N. Vaenas, O. S. Game, T. J. Routledge, M. Wong-Stringer, C. Rodenburg and D. G. Lidzey, *ACS Applied Materials & Interfaces*, 2018, **10**, 39428–39434.
- 2 J. Su, H. Cai, J. Yang, X. Ye, R. Han, J. Ni, J. Li and J. Zhang, *ACS Appl. Mater. Interfaces*, 2019, **12**, 3531–3538.
- 3 J. E. Bishop, C. D. Read, J. A. Smith, T. J. Routledge and D. G. Lidzey, *Scientific Reports*, 2020, **10**, 6610.
- 4 H. Cai, X. Liang, X. Ye, J. Su, J. Guan, J. Yang, Y. Liu, X. Zhou, R. Han, J. Ni, J. Li and J. Zhang, *ACS Applied Energy Materials*, 2020, **3**, 9696–9702.
- 5 J. Su, X. Zheng, H. Guo, S. Jiang, H. Tian, J. Yang, X. Ye, H. Cai, J. Ni, J. Qiu and J. Zhang, *Journal of Electronic Materials*, 2022, **51**, 2396–2405.
- 6 M. Park, S. C. Hong, Y. W. Jang, J. Byeon, J. Jang, M. Han, U. Kim, K. Jeong, M. Choi and G. Lee, *International Journal of Precision Engineering and Manufacturing - Green Technology*, 2022, 1–12.
- 7 A. T. Barrows, A. J. Pearson, C. K. Kwak, A. D. F. Dunbar, A. R. Buckley and D. G. Lidzey, *Energy and Environmental Science*, 2014, **7**, 2944–2950.
- 8 M. Ramesh, K. M. Boopathi, T. Y. Huang, Y. C. Huang, C. S. Tsao and C. W. Chu, *ACS Applied Materials and Interfaces*, 2015, **7**, 2359–2366.
- 9 D. K. Mohamad, J. Griffin, C. Bracher, A. T. Barrows and D. G. Lidzey, *Advanced Energy Materials*, 2016, **6**, 1–7.
- 10 S. C. Hong, G. Lee, K. Ha, J. Yoon, N. Ahn, W. Cho, M. Park and M. Choi, *ACS Applied Materials & Interfaces*, 2017, **9**, 7879–7884.
- 11 S. Bag, J. R. Deneault and M. F. Durstock, *Advanced Energy Materials*, 2017, **7**, 1–11.
- 12 J. Yao, L. Yang, F. Cai, Y. Yan, R. S. Gurney, D. Liu and T. Wang, *Sustainable Energy Fuels*, 2018, **2**, 436–443.
- 13 S. Han, H. Kim, S. Lee and C. Kim, *ACS Applied Materials & Interfaces*, 2018, **10**, 7281–7288.
- 14 L.-H. Chou, X.-F. Wang, I. Osaka, C.-G. Wu and C.-L. Liu, *ACS Appl. Mater. Interfaces*, 2018, **10**, 38042–38050.
- 15 M. Park, W. Cho, G. Lee, S. C. Hong, M. cheol Kim, J. Yoon, N. Ahn and M. Choi, *Small*, 2019, **15**, 1–7.
- 16 Y. S. Chou, L. H. Chou, A. Z. Guo, X. F. Wang, I. Osaka, C. G. Wu and C. L. Liu, *ACS Sustainable Chemistry and Engineering*, 2019, **7**, 14217–14224.
- 17 L. H. Chou, Y. T. Yu, X. F. Wang, I. Osaka, C. G. Wu and C. L. Liu, *Energy Technology*, 2020, **8**, 1–7.
- 18 N. Rolston, W. J. Scheideler, A. C. Flick, J. P. Chen, H. Elmaraghi, A. Sleugh, O. Zhao, M. Woodhouse and R. H. Dauskardt, *Joule*, 2020, **4**, 2675–2692.
- 19 A. Z. Guo, L. H. Chou, S. H. Yang, D. Wang, X. F. Wang, I. Osaka, H. W. Lin and C. L. Liu, *Advanced Materials Interfaces*, 2021, **8**, 1–9.
- 20 L. H. Chou, Y. T. Yu, I. Osaka, X. F. Wang and C. L. Liu, *Journal of Power Sources*, 2021, **491**, 229586.

- 21 T.-W. Chen, S. N. Afraj, S.-H. Hong, L.-H. Chou, A. Velusamy, C.-Y. Chen, Y. Ezhumalai, S.-H. Yang, I. Osaka, X.-F. Wang, M.-C. Chen and C.-L. Liu, *ACS Applied Energy Materials*, 2022, **5**, 4149–4158.
- 22 E. J. Cassella, E. L. K. Spooner, T. Thornber, M. E. O’Kane, T. E. Catley, J. E. Bishop, J. A. Smith, O. S. Game and D. G. Lidzey, *Advanced Science*, 2022, **9**, 2104848.
- 23 J. Silvano, S. Hamtaei, P. Verding, B. Vermang and W. Deferme, *ACS Appl. Energy Mater.*, 2023, **6**, 7363–7376.
- 24 J. Zhao, X. Yang, W. Zhou, R. Wang, Y. Wang, J. Zhang, X. Zhong, H. Ren, G. Hou, Y. Ding, Y. Zhao and X. Zhang, *ACS Appl. Energy Mater.*, 2024, **7**, 3540–3549.
- 25 V. D. Mihailescu, J. Wildeman and P. W. M. Blom, *Phys. Rev. Lett.*, 2005, **94**, 126602.
- 26 T. Kirchartz, F. Deledalle, P. S. Tuladhar, J. R. Durrant and J. Nelson, *J. Phys. Chem. Lett.*, 2013, **4**, 2371–2376.
- 27 W. H. K. Perera, M. G. Masteghin, H. Shim, J. D. Davies, J. L. Ryan, S. J. Hinder, J. S. Yun, W. Zhang, K. D. G. I. Jayawardena and S. R. P. Silva, *Solar RRL*, 2023, **2300388**, 1–11.
- 28 Y. Wang, X. Liu, Z. Zhou, P. Ru, H. Chen, X. Yang and L. Han, *Advanced Materials*, 2019, **31**, 1803231.
- 29 J. A. Christians, J. S. Manser and P. V. Kamat, *J. Phys. Chem. Lett.*, 2015, **6**, 852–857.
- 30 S. N. Habisreutinger, N. K. Noel and H. J. Snaith, *ACS Energy Lett.*, 2018, **3**, 2472–2476.
- 31 P. Caprioglio, C. M. Wolff, O. J. Sandberg, A. Armin, B. Rech, S. Albrecht, D. Neher and M. Stolterfoht, *Advanced Energy Materials*, 2020, **10**, 2000502.